Advances in Water Resources 79 (2015) 140–152

Contents lists available at ScienceDirect

Advances in Water Resources

journal homepage: www.elsevier.com/locate/advwatres

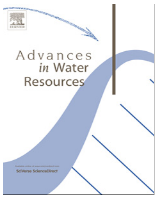

Combined effect of rheology and confining boundaries on spreading of gravity currents in porous media

Sandro Longo [a,*], Valentina Ciriello [b], Luca Chiapponi [a], Vittorio Di Federico [b]

[a] Dipartimento di Ingegneria Civile, Ambiente Territorio e Architettura (DICATeA), Università di Parma, Parco Area delle Scienze, 181/A, 43124 Parma, Italy
[b] Dipartimento di Ingegneria Civile, Chimica, Ambientale e dei Materiali (DICAM), Università di Bologna, Viale Risorgimento, 2, 40136 Bologna, Italy

ARTICLE INFO

Article history:
Received 28 November 2014
Received in revised form 24 February 2015
Accepted 27 February 2015
Available online 11 March 2015

Keywords:
Porous
Gravity current
Similarity solution
Channel shape
Non-Newtonian
Laboratory experiments

ABSTRACT

One-dimensional flows of gravity currents within horizontal and inclined porous channels are investigated combining theoretical and experimental analysis to evaluate the joint effects of channel shape and fluid rheology. The parameter β governs the shape of the channel cross section, while the fluid rheology is characterised by a power-law model with behaviour index n. Self-similar scalings for current length and height are obtained for horizontal and inclined channels when the current volume increases with time as t^{α}.

For horizontal channels, the interplay of model parameters α, n, and β governs the front speed, height, and aspect ratio of the current (ratio between the average height and the length). The dependency is modulated by two critical values of $\alpha, \alpha_{\beta} = n/(n+1)$ and $\alpha_n = (2\beta+1)/\beta$. For all channel shapes, α_{β} discriminates between currents whose height decreases ($\alpha < \alpha_{\beta}$) or increases ($\alpha > \alpha_{\beta}$) with time at a particular point. For all power-law fluids, α_n discriminates between decelerated currents, with time-decreasing aspect ratio ($\alpha < \alpha_n$), and accelerated currents, with time-increasing aspect ratio ($\alpha > \alpha_n$). Only currents with time-decreasing height ($\alpha < \alpha_{\beta}$) and aspect ratio ($\alpha < \alpha_n$) respect model assumptions asymptotically; the former constraint is more restrictive than the latter.

For inclined channels, a numerical solution in self-similar form is obtained under the hypothesis that the product of the channel inclination θ and the slope of the free-surface is much smaller than unity; this produces a negligible error for $\theta > 2^{\circ}$, and is acceptable for $\theta > 0.5^{\circ}$. The action of gravity in inclined channels is modulated by both the behaviour index n and the shape factor β. For constant flux, the current reaches at long times a steady state condition with a uniform thickness profile. In steep channels and for sufficiently long currents, the free-surface slope becomes entirely negligible with respect to channel inclination, and the constant thickness profile depends only on n.

Theoretical results are validated by comparison with experiments (i) in horizontal and inclined channels with triangular or semicircular cross-section, (ii) with different shear-thinning fluids, and (iii) for constant volume and constant flux conditions. The experimental results show good agreement with theoretical predictions in the long-time regime.

Our analysis demonstrates that self-similar solutions are able to capture the essential long-term behaviour of gravity currents in porous media, accounting for diverse effects such as non-Newtonian rheology, presence of boundaries, and channel inclination. This provides a relatively simple framework for sensitivity analysis, and a convenient benchmark for numerical studies.

1. Introduction

Gravity currents are responsible for many natural processes occurring in the atmosphere, water bodies and the subsurface, as whenever two fluids of different density come in contact, the gravity action favours their relative motion. The interest in gravity currents has generated a vast literature, including theoretical, numerical and experimental studies (e.g. [1,2] and references therein). Gravity currents in porous media involve the spreading of a fluid in a natural or artificial domain saturated with another fluid of a different density; the pressure/buoyancy driving is balanced by viscous adjustment of the fluid in the pore space. This phenomenon has been studied in connection with environmental and industrial applications such as aquifer remediation [3,4], carbon sequestration [5], saltwater intrusion [6], and well drilling [7].

---

* Corresponding author.

http://dx.doi.org/10.1016/j.advwatres.2015.02.016

Earlier studies [8–10] have addressed the one-directional propagation of gravity currents driven by gradients in hydrostatic pressure (horizontal bed) or gravity (inclined bed) in homogeneous domains with simple geometry. Further complexity in the flow description arises when either heterogeneity in medium properties or topographic control is present in the flow domain, as suggested by diverse applicative contexts, such as modelling of carbon dioxide injection in natural reservoirs [11].

Within medium heterogeneity, Ciriello et al. [12] considered the influence of vertical and horizontal permeability variations on the propagation of planar currents. Zheng et al. [13,14] further extended the study of gravity driven flows in elongated porous domains, by considering: (i) coupled permeability and porosity gradients parallel and transverse to the flow direction; (ii) currents propagating away or towards the domain origin, giving rise to different types of self-similar behaviour. These studies showed that macro-heterogeneity in medium properties alters both the extension and the shape of the intruding current.

As for topographic control, Golding and Huppert [15] investigated the effect of confining boundaries on one-dimensional gravity-driven flow in porous channels, by considering a uniform cross-section with shape described by one parameter. The propagation rate is affected by channel shape in a way depending on the time exponent of the current volume; when the channel has a slope much steeper than its free surface, the spreading rate is unaffected by confining boundaries. Pegler et al. [16] analysed the effect of an upward sloping topography in the flow direction on constant flux currents. Topography was shown to control the early or late-time evolution of the current, depending on the shape of the lower boundary over which the current flows.

The rheology of the intruding fluid is another key factor in controlling the propagation of gravity currents in porous media [17,18]. In some cases the ambient and current fluids may be appropriately described as Newtonian, but in many instances, one or both fluids behave as non-Newtonian; relevant cases include polymer solutions, heavy oils, surfactants, foams, gels, emulsions, greases, and water-based slurries used for aquifer remediation [19]. The rheology of non-Newtonian fluids of interest in porous media flow encompasses several possible models [20]; among these, the power-law model provides the simplest relationship between stress and strain, and constitutes an acceptable approximation when: (i) the fluid is purely viscous; (ii) yield stresses are negligible, (iii) no other physical effects, such as adsorption, are present; (iv) the fluid rheologic parameters are evaluated in the range of shear rates occurring in the medium at the pore scale [21,22].

The impact of heterogeneity in porous medium properties is particularly relevant for non-Newtonian flow, as suggested by the numerical simulations of Fadili et al. [23], who showed that in correlated media streamlines of shear-thinning flow tend to concentrate along higher permeability paths. To explore the combined effect of fluid rheology and spatial heterogeneity, Di Federico et al. [24] derived a closed-form solution for radial gravity currents of power-law fluids in porous media with a deterministic permeability variation along the vertical; the solution was then validated experimentally. The axisymmetric scheme describes the motion of a gravity current originating from a single vertical borehole and spreading in an infinite domain. For currents propagating in narrow, elongated domains, topographic features may control the flow, yet to the best of our knowledge the effect of topographic control on non-Newtonian gravity currents has never been explored.

To this end, we firstly investigate in this work the combined effect of power-law rheology and confining boundaries on the motion of gravity currents in porous media. The boundary effect is represented by means of a channel of constant cross-section along the lines of Golding and Huppert [15], with the intruding fluid flowing (i) at the impervious bottom, for currents denser than the ambient fluid, or (ii) at the impervious cap, for currents lighter than the ambient fluid. In both cases, the confined porous channel can be horizontal or inclined. A limiting case of channels engraved in impervious boundaries is represented by fractures and very narrow cross-section channels. This scenario was analysed for low-Reynolds number flows by Takagi and Huppert [25,26] for Newtonian fluids, and by Longo et al. [27] for shear-thinning fluids. The presence of porous material inside these fractures strongly influences flow behaviour [26].

In the following sections we first present the theoretical model partially introduced by Ciriello et al. [28] for the limited case of horizontal channels and here extended to the inclined case. Both cases are discussed in detail, focusing on sensitivity to model parameters and range of applicability of the proposed formulation. Then an extended set of laboratory experiments is presented and discussed in order to validate the theoretical formulation under diverse possible scenarios, including: (i) different fluids; (ii) channels of different shape; (iii) horizontal or inclined channels; (iv) constant volume or constant flux injection. A set of conclusions closes the paper.

2. Problem formulation

Consider a non-Newtonian fluid with rheology described by the classical power-law model relating shear stress τ and shear rate $\dot{\gamma}, \tau = \widetilde{\mu}\dot{\gamma}|\dot{\gamma}|^{n-1}$, having parameters $\widetilde{\mu}$ (consistency index) and n (fluid behaviour index). This fluid, of density $\rho + \Delta\rho$, is released at the origin of a straight channel of uniform inclination θ as depicted in Fig. 1. The channel is filled with a homogeneous porous medium saturated with a lighter fluid of density ρ. Under this scenario, a gravity current is generated, advancing in a condition of vertical equilibrium with hydrostatic pressure distribution. The height of the current is much smaller than its length, with consequent negligible vertical velocities. Surface tension effects and mixing at fluids interface are also unimportant. The channel cross-section is symmetric and described by a power-law relationship: $b(y) = ra(y/a)^{\beta}$, where β is a shape parameter, a a length associated with the channel width, and r a dimensionless constant. For wide cross sections with $\beta > 1$, the current is taken to occupy only a small portion of the channel, so that $h \ll a$. Note that: (i) the case $\beta = 1$ corresponds to a triangular cross-section with $r = \cot\chi$, being 2χ the vertex angle; (ii) the case $\beta = 2$ approximates a semicircular cross-section as the height of the current is limited compared to the cross section radius $a/2$; (iii) the case $\beta \to \infty$ corresponds to a rectangular channel of half width a; as $h \ll a$, two-dimensional flow on a flat surface is recovered.

Our model relies on (i) local mass balance, (ii) a 1-D seepage formula extending Darcy's law to the case of non-Newtonian fluid flow (e.g. [17]). These two equations read, respectively

$$\phi\frac{\partial}{\partial t}\left(A_c h^{(\beta+1)/\beta}\right) + \frac{\partial}{\partial x}\left(u_x A_c h^{(\beta+1)/\beta}\right) = 0 \tag{1}$$

$$u_x(x,t) = -(\Lambda\Delta\rho g)^{1/n}k^{(1+n)/(2n)}\left(\frac{\partial h}{\partial x}\cos\theta - \sin\theta\right)^{1/n}, \tag{2}$$

where ϕ is the porosity, k the medium permeability, $A_c = \frac{2\beta}{\beta+1}\frac{a^{(\beta-1)/\beta}}{r^{1/\beta}}$, and $\Lambda = \frac{8^{(n+1)/2}}{2}\left(\frac{n}{3n+1}\right)^n\frac{\phi^{(n-1)/2}}{\widetilde{\mu}}$. Substituting (2) in (1) and introducing the natural velocity scale $v^* = \frac{(\Lambda\Delta\rho g)^{1/n}k^{(1+n)/(2n)}}{\phi}$ yields

$$\frac{\partial h^{F_1}}{\partial t} + v^*(\sin\theta)^{1/n}\frac{\partial}{\partial x}\left[h^{F_1}\left(1 - \cot\theta\frac{\partial h}{\partial x}\right)^{1/n}\right] = 0, \tag{3}$$

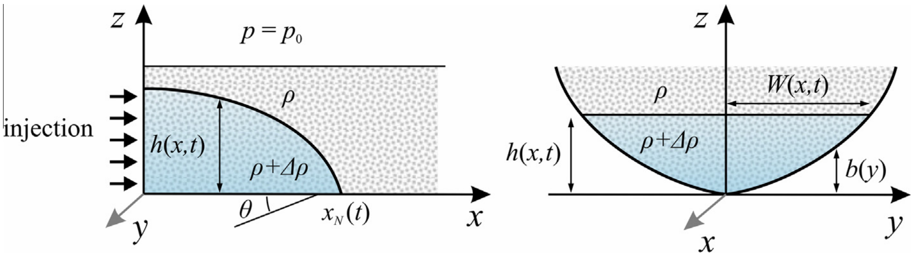

Fig. 1. A sketch of the system with the coordinates and the cross-section in the $y-z$ plane.

where $F_1=\frac{\beta+1}{\beta}$ is a cross-section shape factor, reducing to unity for plane geometry. The local mass balance expressed by Eq. (3) is complemented by the global continuity equation, written in the form

$$\phi\int_0^{x_N(t)} A_c h^{F_1}\,dx = qt^{\alpha}, \tag{4}$$

in which α and q (dimensions $[\mathrm{L}^3\mathrm{T}^{-\alpha}]$) are positive constants and $x_N(t)$ is the front end of the current. Note that $\alpha=0$ and $\alpha=1$ indicate the instantaneous release of a fixed volume and a constant volume flux, respectively. The problem formulation is completed by the constraint of vanishing height at the current front, i.e.

$$h(x_N(t),t)=0. \tag{5}$$

3. Horizontal channels

3.1. Solution

Horizontal channels represent a particular application of the proposed model. This configuration has been introduced and preliminarily discussed by Ciriello et al. [28]. Here, we recover the main concepts of this case to explore the results in greater depth and compare them with those associated with inclined channels. In the horizontal configuration, Eq. (3) reduces to

$$\frac{\partial h^{F_1}}{\partial t}+v^*\frac{\partial}{\partial x}\left[h^{F_1}\left(-\frac{\partial h}{\partial x}\right)^{1/n}\right]=0. \tag{6}$$

Upon introducing the time and space scales $t^*=\left(\frac{q}{\phi v^{*3}}\right)^{1/(3-\alpha)}$, $x^*=v^*t^*$, (6) and (4) become

$$\frac{\partial \tilde{h}^{F_1}}{\partial \tilde{t}}+\frac{\partial}{\partial \tilde{x}}\left[\tilde{h}^{F_1}\left(-\frac{\partial \tilde{h}}{\partial \tilde{x}}\right)^{1/n}\right]=0, \tag{7}$$

$$\int_0^{\tilde{x}_N(\tilde{t})}\tilde{A}_c\tilde{h}^{F_1}\,d\tilde{x}=\tilde{t}^{\alpha}, \tag{8}$$

where $\tilde{A}_c=\frac{2\beta}{\beta+1}\frac{1}{r^{1/\beta}}\left(\frac{a}{x^*}\right)^{(\beta-1)/\beta}$, while the boundary condition (5) is unchanged in dimensionless form.

Hereinafter the tilde, indicating a non dimensional variable, is removed. Note that for $\alpha=3$, the time scale t^* defined above is invalid, and a new, arbitrary one t^{**} has to be defined; a second velocity scale v^{**}, proportional to $q^{1/3}$, emerges beyond v^* defined above. The dimensionless formulation of the equations for $\alpha=3$ thus includes a new parameter δ, equal to the ratio between the two velocity scales v^* and v^{**}. Mathematical details can be found in [10,22,24].

Eqs. (7) and (8) provide the scaling of the current length and height and suggest the following solution form and self-similar variable

$$h(x,t)=A_c^{-(n+1)F_4}\eta_N^{F_5}t^{F_3}\Psi(\zeta),\quad \eta=A_c^{F_4}x/t^{F_2},\quad \zeta=\frac{\eta}{\eta_N}, \tag{9}$$

where η_N is the value of the similarity variable at the current front, $\Psi(\zeta)$ is the shape function, and ζ is the reduced similarity variable. The position of the current front is given by

$$x_N(t)=\frac{\eta_N}{A_c^{F_4}}t^{F_2}. \tag{10}$$

The exponents are $F_2=\frac{\alpha\beta+(\beta+1)n}{(\beta+1)(n+1)+\beta}$, $F_3=\frac{\beta[\alpha(n+1)-n]}{(\beta+1)(n+1)+\beta}$, $F_4=\frac{\beta}{(\beta+1)(n+1)+\beta}$, $F_5=n+1$. For $n=1$ (Newtonian fluid) and any β, the formulation reduces to $F_2=\frac{\alpha\beta+\beta+1}{3\beta+2}$, $F_3=\frac{\beta(2\alpha-1)}{3\beta+2}$, $F_4=\frac{\beta}{3\beta+2}$, $F_5=2$; these results coincide with those of Golding and Huppert [15]. For $\beta\to\infty$ and any n, the two-dimensional problem of Di Federico et al. [17] is recovered; in this case the exponents simplify to $F_1=1, F_2=\frac{\alpha+n}{n+2}, F_3=\frac{\alpha(n+1)-n}{n+2}, F_4=\frac{1}{n+2}$, while $F_5=n+1$. For $\beta\to\infty$ and $n=1$ (plane porous flow of a Newtonian fluid), the problem reduces to one of the special cases examined by Huppert and Woods [8] and $F_1=1, F_2=\frac{\alpha+1}{3}, F_3=\frac{2\alpha-1}{3}, F_4=\frac{1}{3}, F_5=2$. Substituting Eq. (9) in Eqs. (7) and (8) and in the dimensionless form of Eq. (5) yields

$$\frac{d}{d\zeta}\left[\Psi^{F_1}\left(-\frac{d\Psi}{d\zeta}\right)^{1/n}\right]-F_1\Psi^{F_1-1}\left(F_2\frac{d\Psi}{d\zeta}-F_3\Psi\right)=0, \tag{11}$$

$$\eta_N=\left(\int_0^1\Psi^{F_1}d\zeta\right)^{-F_4}, \tag{12}$$

$$\Psi(1)=0. \tag{13}$$

For $\alpha=0$ the set of Eqs. (11)–(13) has a closed form solution given by

$$\Psi(\zeta)=\frac{F_{20}^n}{n+1}\left(1-\zeta^{F_5}\right),\quad \eta_N=\left[\frac{F_5^{F_1}}{F_1F_4F_{20}^{nF_1}}\frac{\Gamma(1/(F_4F_5))}{\Gamma(1/F_5)\Gamma(F_1)}\right]^{F_4}, \tag{14}$$

where $F_{20}=F_2(\alpha=0)\equiv\frac{(\beta+1)n}{(\beta+1)(n+1)+\beta}$ and $\Gamma(.)$ is the Gamma function. For $n=1$ the time exponent of the length of a current of constant volume reduces to $F_{20}=2/5$ for triangular channels ($\beta=1$), and to $F_{20}=3/8$ for nearly semicircular channels ($\beta=2$). For $\alpha\neq0$ the set of Eqs. (11)–(13) needs to be solved numerically.

The left panel of Fig. 2 depicts the shape factor against the reduced similarity variable for different values of α and n. The shape factor increases for increasing α, and is larger for shear thinning than for shear thickening fluids; this difference decreases with increasing α. Upon plotting the prefactor η_N versus β (right panel of Fig. 2), it is seen that this dimensionless quantity decreases with α, and is weakly dependent on the cross sectional shape for $\beta\geqslant1$; the dependence is stronger for narrow cross sections ($\beta<1$). The influence of n on η_N is also relatively minor.

To understand how these results impact dimensional quantities of interest, Fig. 3 shows the thickness of the current at different times in a channel of circular cross section; flow of three fluids with different flow behaviour index n and the same value of consistency index $\tilde{\mu}$ is considered. Results are shown for $\alpha=0$ (constant volume) and $\alpha=1.0$ (constant volume flux). It is seen that

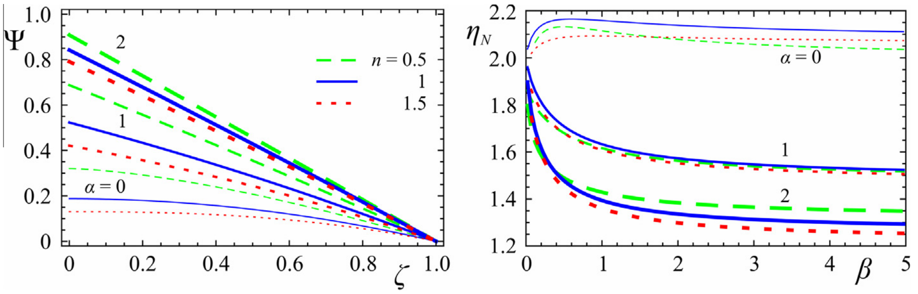

Fig. 2. Left panel: shape function for a circular horizontal channel ($\beta = 2$) for $\alpha = 0$ (thin curves), $\alpha = 1$ (curves), and $\alpha = 2$ (thick curves) and for $n = 0.5, 1, 1.5$. Right panel: the prefactor η_N as a function of the cross-section shape for various values of α and n.

increasing n generates a shorter current, especially at early times. Asymptotically, the difference in length becomes negligible for $\alpha = 0$, while it is more evident for $\alpha = 1.0$. Increasing the consistency index, or reducing the medium permeability and the fluid density, reduces the extension of the current (not shown here).

3.2. Discussion

The exponents F_2 and F_3 govern the time change of the current radius and height, respectively. While F_2 is always positive, Eq. (10) implies that the current front is accelerated, decelerated or moves at constant speed depending whether $F_2 > 1, F_2 < 1$ or $F_2 = 1$, respectively. Similarly, Eq. (9) entails a time increase of the current thickness at a given location for $F_3 > 0$, and a decrease for $F_3 < 0$. Taking the spatial average of the current thickness over its length x_N, and dividing by x_N, shows that the current aspect ratio $\overline{h}/x_N$ (where the overbar indicates the spatial average) is proportional to time raised to the power $F_3 - F_2$. Hence the current aspect ratio increases or decreases over time, depending on the sign of $F_3 - F_2$. The same dependence on time is found for the average free-surface gradient $\overline{(\partial h)/(\partial x)}$ driving the motion.

The sign of the time exponents $F_2 - 1, F_3$, and $F_3 - F_2$ is studied by deriving the critical value of α, above which each exponent is positive. Table 1 reports the values of $F_2 - 1, F_3$ and $F_3 - F_2$ in the first column, and lists the respective conditions on α in the second column. Only two critical values of α emerge, $\alpha_\beta = n/(n+1)$ and $\alpha_n = (2\beta + 1)/\beta$, as the conditions for the positivity of $F_2 - 1$ and $F_3 - F_2$ are equal. This is so because an accelerated current is driven by a pressure gradient increasing over time.

The dependence of the time exponents $F_2 - 1, F_3$, and $F_3 - F_2$ on model parameters is then studied systematically by taking their partial derivatives with respect to α, n, and β. Note that the type of dependence resulting for $F_2 - 1$ is valid also for F_2. Columns three to five of Table 1 list the conditions under which each exponent increases with α, n, and β, respectively. It is seen that all exponents are increasing functions of α; as the current volume increases more rapidly with time, so do the current length and speed, thickness at a given location, and aspect ratio. Furthermore, the partial derivatives of all the exponents with respect to β and n are null for $\alpha = \alpha_\beta$ and $\alpha = \alpha_n$, respectively. This implies that the two critical values of α previously determined, α_β and α_n, govern also the dependence of the exponents on the channel shape and fluid rheology, parameterised, respectively, by β and n.

Table 1
Value and behaviour of time exponents for horizontal channels. Row 1: Current speed $F_2 - 1$. Row 2: Current thickness F_3. Row 3: Current aspect ratio $F_3 - F_2$. Rows 4 and 5: critical values α_β and α_n. Column 1: value of the exponent. Column 2: condition for exponent > 0. Column 3: condition for exponent increasing with α. Column 4: condition for exponent increasing with n. Column 5: condition for exponent increasing with β.

Exponent	Value	> 0	$\frac{\partial}{\partial\alpha} > 0$	$\frac{\partial}{\partial n} > 0$	$\frac{\partial}{\partial\beta} > 0$
$F_2 - 1$	$\frac{\alpha\beta - 2\beta - 1}{(\beta+1)(n+1)+\beta}$	$\alpha > \alpha_n$	$\forall\alpha, n, \beta$	$\alpha < \alpha_n$	$\alpha > \alpha_\beta$
F_3	$\frac{\beta[\alpha(n+1) - n]}{(\beta+1)(n+1)+\beta}$	$\alpha > \alpha_\beta$	$\forall\alpha, n, \beta$	$\alpha > \alpha_n$	$\alpha > \alpha_\beta$
$F_3 - F_2$	$\frac{n(\alpha\beta - 2\beta - 1)}{(\beta+1)(n+1)+\beta}$	$\alpha > \alpha_n$	$\forall\alpha, n, \beta$	$\alpha > \alpha_n$	$\alpha > \alpha_\beta$
α_β	$\frac{n}{n+1}$				
α_n	$\frac{2\beta+1}{\beta}$				

When $\alpha = \alpha_\beta$, the time exponents become independent of β, as $F_2 = n/(n+1), F_3 = 0$, and $F_3 - F_2 = -n/(n+1)$; thus α_β discriminates between subcritical ($\alpha < \alpha_\beta$) and supercritical ($\alpha > \alpha_\beta$) currents, whose thickness respectively decreases or increases with time at a particular point. This is a consequence of mass conservation, as only for a supercritical current the volume increase is rapid enough to compensate for the length increase with time. Further, it is noted that all exponents decrease with increasing β for $\alpha < \alpha_\beta$; the reverse is true for $\alpha > \alpha_\beta$. To explain the behaviour

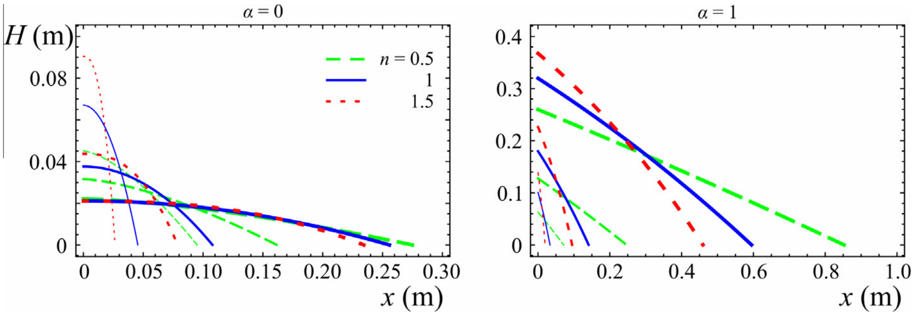

Fig. 3. Current thickness at times $t = 10$ s (thin curves), $t = 100$ s (curves), and $t = 1000$ s (thick curves) in a circular horizontal channel ($\beta = 2$) of radius 0.095 m, filled with a medium with $d = 2$ mm, $\phi = 0.38$; fluid properties are $\rho_c = 1080$ kg m^{-3}, $\tilde{\mu} = 0.14$ Pa s^{-n}, and $n = 0.5, 1.0, 1.5$. Left panel: $\alpha = 0$, volume $q = 100$ ml. Right panel: $\alpha = 1$, volume flux $q = 10$ ml s^{-1}.

of F_3, we note that for any α, the current distributes the total volume at given time between an increase in length and a variation in thickness. For subcritical currents, the increase in length is more important, as the thickness decreases over time; for supercritical currents, the variation in thickness is more important, as the thickness increases over time. Hence, it is more efficient for a supercritical current to distribute the incoming volume over positive thickness variations than over length increases. As the channel volume per unit length is larger for flatter cross sections (larger β), the exponent F_3 increases with increasing β. Conversely, F_3 decreases with increasing β for subcritical currents. The tendency of thickness variations to prevail over length increases for supercritical currents ($\alpha > \alpha_\beta$) is confirmed by the behaviour of the exponent F_2. As already noted, F_2 behaves similarly to F_3, but it results $\partial F_3/\partial\beta > \partial F_2/\partial\beta$ if $\alpha > \alpha_\beta$ (as suggested by the positiveness of $\partial(F_3 - F_2)/\partial\beta$ if $\alpha > \alpha_\beta$ in Table 1). This indicates that the average spatial gradient of the current thickness increases over time for $\alpha > \alpha_\beta$, even though at a reduced rate for increasing β.

A comparison with analogous results obtained for free-surface viscous flow in open channels without porous media by Longo et al. [27] reveals that while α_β has the same value $n/(n+1)$, the dependency of F_2 on β is not monotonic as implied by Table 1 for porous currents, but that F_2 attains its minimum or maximum value in triangular channels with $\beta = 1$, depending whether $\alpha < \alpha_\beta$ or $\alpha > \alpha_\beta$. This partial analogy in physical behaviour was explained for Newtonian currents by Golding and Huppert [15], who noted that the common value of α_β stems from mass balance considerations, that hold true for porous and free-surface gravity currents alike. The qualitative difference in behaviour for narrow cross sections is explained by the adoption of the Darcy and Stokes equation for the porous and non-porous case, respectively.

When $\alpha = \alpha_n$, the time exponents become independent of n, as $F_2 = 1, F_3 = 1, F_3 - F_2 = 0$. Hence α_n discriminates between currents whose aspect ratio decreases ($\alpha < \alpha_n$) or increases ($\alpha > \alpha_n$) with time. Correspondingly, the current decelerates or accelerates, driven by an average spatial pressure gradient decreasing or increasing with time. When $\alpha < \alpha_n$, a larger n implies an increase of F_2 and a decrease of F_3 and $F_3 - F_2$; the reverse is true for $\alpha > \alpha_n$. Physically, a decelerating current ($\alpha < \alpha_n$) implies that the shear applied to the fluid decreases over time. For a shear thinning fluid ($n < 1$), this entails an increased resistance to flow, as the apparent viscosity increases with decreasing shear stress. The opposite effect happens with a shear thickening fluid ($n > 1$): the apparent viscosity decreases with decreasing shear stress, hence the resistance to flow decreases over time. As a result, decelerating currents of shear-thickening fluids have a larger F_2 and a smaller F_3 than decelerating currents of shear-thinning fluids. The behaviour is the opposite for a accelerating currents ($\alpha > \alpha_n$), for which the shear applied to the fluid increases over time.

The two critical values of α shown in Table 1 are themselves function of problem parameters n and β. Upon analysing their dependence on flow behaviour index and cross sectional shape, we note that:

- α_β is controlled by rheology, and is an increasing function of n. It tends to 0 for $n \to 0$; it takes a value $\approxeq 0.25$ for a very shear thinning fluid with $n = 0.3$, increasing to 0.5 for a Newtonian fluid, and reaching a value of 0.6 for a very shear thickening fluid with $n = 1.5$. For the theoretical case $n \to \infty, \alpha_\beta \to 1$. Physically, α_β is the threshold value of α beyond which the current height increases with time at a given point. As the fluid behaviour index n increases, so does the resistance to flow. Hence for larger values of n, more fluid is required to maintain an increase in the thickness of the current; thus the threshold value α_β is larger.
- α_n is controlled by channel shape, and decreases as the cross section becomes flatter (β increases), varying from values larger than 3 for narrow cross sections with $\beta < 1$ to 3 for a triangular cross section with $\beta = 1$, and reaching the limit value of 2 for wide rectangular channels ($\beta \to \infty$). Physically, α_n is the threshold value of α to be exceeded to maintain accelerated currents with time increasing aspect ratio. As β increases, so does the volume required to fill a given cross section. Hence by virtue of mass balance the current length will be shorter, and the threshold value of α needed to observe an accelerated current will decrease.

Summarizing the previous discussion, it can be seen that distinct ranges of α are associated with different behaviours, depending whether the current has time decreasing or time increasing thickness ($\alpha \lesseqgtr \alpha_\beta$), and is decelerated or accelerated ($\alpha \lesseqgtr \alpha_n$). Irrespective of fluid nature and channel shape, the two threshold values of α are such that $\alpha_\beta < \alpha_n$. Hence, the following flow regimes are observed: (i) in the range $\alpha \leqslant \alpha_\beta$, the current is decelerated ($F_2 - 1 < 0$), and its thickness does not increase with time ($F_3 \leqslant 0$); (ii) for $\alpha_\beta < \alpha \leqslant 2$, the current is decelerated ($F_2 - 1$ is still negative) and its thickness increases with time ($F_3 > 0$), as it does for larger α values; (iii) for $2 < \alpha \leqslant 3$, the current is decelerated in narrow cross sections with $\beta < 1$ (since $F_2 - 1 < 0$), while it may be decelerated or accelerated depending on channel shape β in wide cross sections with $\beta \geqslant 1$; (iv) for $\alpha > 3$, the current is accelerated in wide cross sections with $\beta \geqslant 1$ (since $F_2 - 1 > 0$), while it may be decelerated or accelerated in narrow cross sections with $\beta < 1$.

To better grasp the behaviour of F_2, F_3, and $F_3 - F_2$, these exponents are shown in Fig. 4(a), (c) and (e) as a function of β for fixed $n = 0.5$ and in Fig. 4(b), (d) and (f) as a function of n for fixed $\beta = 2$; results for various values of α are shown. The two reference values ($n = 0.5$ and $\beta = 2$) represent common cases in natural settings, i.e. a shear-thinning fluid and a nearly semicircular cross section. A more complete overview of results is shown in the Supplementary Material, where the behaviour of the exponents F_2, F_3, and $F_3 - F_2$ is depicted as a function of β for $n = 0.5, 1, 1.5$, and as a function of n for $\beta = 0.5, 1, 2$. It is observed that variations of the channel shape bring about significant changes in the key time exponents in the range $0 < \beta \leqslant 2$; this effect is compounded for larger values of n. Results are less sensitive to β for $\beta > 3$, as the change in cross sectional area corresponding to variations of β is relatively minor in this range. The influence of n on the exponents is larger for shear-thinning than for shear-thickening fluids, as the change in apparent viscosity is proportionately larger for lower values of n.

The previous analysis allows evaluating the constraints placed on the value of problem parameters by model assumptions. Two limitations emerge when considering the large time asymptotic behaviour of the current:

- The average space gradient must be limited in order to satisfy the thin current approximation, as large gradients induce non negligible vertical components of the velocity, making the vertical equilibrium hypothesis and the Dupuit approximation unacceptable. This implies a time decreasing aspect ratio, i.e. $F_3 - F_2 < 0$, or equivalently $\alpha < \alpha_n$. However, the limitation is somewhat relaxed by two effects: (i) vertical velocity components in turn favour a reduction of the height and a smoothing of the space gradient; (ii) the invalidity of the Dupuit approximation is a local phenomenon concentrated near the injection zone, with limited effects on the overall current development (see [29]).
- The current thickness at a given point has to decrease with time; otherwise the current profile will eventually exceed the height of the channel cross section, and the current will not

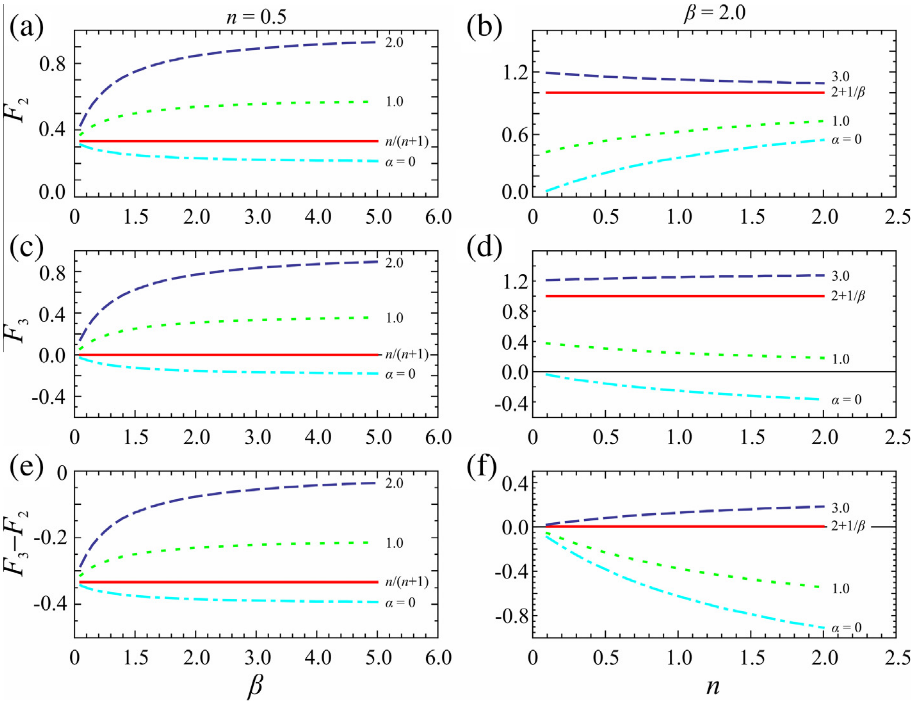

Fig. 4. (a)–(f) Time exponents F_2, F_3 and $F_3 - F_2$ for a current with length $\propto T^{F_2}$, height $\propto T^{F_3}$, aspect ratio/mean free-surface gradient $\propto T^{F_3-F2}$, and volume $\propto T^{\alpha}$ in a porous channel with cross sectional shape parameterized by β. Results are shown for F_2, F_3 and $F_3 - F_2$ in the upper, intermediate and lower rows, respectively, as a function of β for flow behaviour index $n = 0.5$ and as a function of n for $\beta = 2$ (left and right columns, respectively), and for different values of α.

be completely confined by the boundaries. Hence, the finiteness of the channel cross section implies $F_3 \leqslant 0$, or equivalently $\alpha \leqslant \alpha_\beta$.

The second limitation is more stringent, as $\alpha_\beta < \alpha_n$. This was already highlighted for laminar free-surface gravity currents in channels of power-law cross sections [27]. The validity of model assumptions can be also checked preasymptotically following the methodology outlined in Ciriello et al. [12] for a finite time value.

4. Inclined channels

4.1. Solution

For inclined channels, the general formulation of the problem given by Eqs. (3)–(5) is valid, as both the slope of the channel and that of the current drive the flow. Assuming that $\cot\theta \frac{\partial h}{\partial x} \ll 1$, but is not negligible with respect to unity, the following approximation holds,

$$\left(1 - \cot\theta \frac{\partial h}{\partial x}\right)^{1/n} \approx 1 - \frac{1}{n}\cot\theta \frac{\partial h}{\partial x}, \tag{15}$$

and the mass balance Eq. (3) reduces to

$$\frac{\partial h^{F_1}}{\partial t} + v^*(\sin\theta)^{1/n} \frac{\partial}{\partial x}\left[h^{F_1} - \frac{h^{F_1}}{n}\cot\theta \frac{\partial h}{\partial x}\right] = 0. \tag{16}$$

The effective error induced by this approximation will be checked a posteriori. Changing coordinates to the moving frame $x' = x - v^* t(\sin\theta)^{1/n}$, Eqs. (3) and (4) become, respectively:

$$\frac{\partial h^{F_1}}{\partial t} - \frac{v^*}{n}(\sin\theta)^{1/n}\cot\theta \frac{\partial}{\partial x'}\left(h^{F_1}\frac{\partial h}{\partial x'}\right) = 0, \tag{17}$$

$$\phi \int_{-v^* t(\sin\theta)^{1/n}}^{x_N(t) - v^* t(\sin\theta)^{1/n}} A_c h^{F_1} dx' = q t^{\alpha}, \tag{18}$$

and admit a self-similar solution based on the similarity variable and the solution form given by

$$\eta = \frac{x'}{\left(\frac{v^*}{n} h_0 t \cot\theta\ (\sin\theta)^{1/n}\right)^{1/2}}, \quad h = h_0 f(\eta), \tag{19}$$

where h_0 is a constant coefficient.

For a Newtonian fluid ($n = 1$), Golding and Huppert [15] observed that the conservation equation written in the moving frame for an inclined channel (17) is identical to the conservation equation valid for a horizontal channel (6), with v^* changed to $v^*\cos\theta$; hence the action of gravity is not affected by cross-sectional shape. This conclusion cannot be extended to non-Newtonian power-law fluid flow, since Eqs. (6) and (17) differ for $n \neq 1$. Hence for non-Newtonian flow the action of gravity in inclined channels is modulated by both the cross-shape factor F_1 and the fluid behaviour index n.

When the channel inclination is large enough (e.g., $\partial h/\partial x < 0.1\tan\theta$ far from the front end of the current), the current is driven by gravity and the slope of the free surface can be totally neglected. In this case Eq. (15) is equal to unity irrespective of the n value, and Eq. (3) simplifies to

$$\frac{\partial h^{F_1}}{\partial t} + v^*(\sin\theta)^{1/n}\frac{\partial}{\partial x}\left(h^{F_1}\right) = 0. \tag{20}$$

Additionally, the boundary condition (5) cannot be considered as the order of the differential Eq. (20) becomes lower than the general case (1). Eq. (20) admits the trivial solution of a current of constant height with a vertical front. Physically, a smooth transition to null depth is observed at the current front; the rounding of the leading edge is due to the residual effect of the free-surface slope.

Inspection of Eq. (20) shows the scaling $x_N \sim v^* t(\sin\theta)^{1/n}$ for the current length. This result does not depend on the flow parameter α and on the channel shape parameter β, but only on flow behaviour index n. The height scales as $h \sim h_f t^{(\alpha-1)/F_1}$. For $\alpha = 1$, the asymptotic behaviour upstream discussed in Section 4.2 is recovered.

4.2. Constant flux injection

A constant flux gravity current ($\alpha = 1$) represents a special case since the advancement of the nose and the input flux scale like t. For large values of t the current reaches a steady state with uniform thickness, except near the nose (see [8,15]). Mass conservation suggests that the uniform thickness is

$$h_f = \left(\frac{q}{\phi A_c v^*(\sin\theta)^{1/n}}\right)^{1/F_1}. \tag{21}$$

This value is reached asymptotically upstream for $t \to \infty$, whereas near the nose the current height drops to zero with a shape represented by the function $f(\eta)$. Substituting the similarity variables (19) in Eqs. (17) and (18) yields

$$\frac{\partial}{\partial\eta}\left[f^{F_1}\frac{\partial f}{\partial\eta}\right]+\frac{\eta}{2}\frac{\partial f^{F_1}}{\partial\eta}=0,\quad f(\eta_N)=0,\quad \int_{-\infty}^{\eta_N}(1-f)\,d\eta=0, \tag{22}$$

$$\phi h_0^{F_1}\left(\frac{v^*}{n}h_0 t\cot\theta(\sin\theta)^{1/n}\right)^{1/2}A_c\int_{\eta_t}^{\eta_N} f^{F_1}\,d\eta = qt, \tag{23}$$

with

$$\eta_t = -\frac{v^* t(\sin\theta)^{1/n}}{\left(\frac{v^*}{n}h_0 t\cot\theta(\sin\theta)^{1/n}\right)^{1/2}},$$

$$\eta_N = \frac{x_N(t)-v^* t(\sin\theta)^{1/n}}{\left(\frac{v^*}{n}h_0 t\cot\theta(\sin\theta)^{1/n}\right)^{1/2}}, \tag{24}$$

where the integral condition in Eq. (22) is a boundary condition for the function f. The computation of the profile requires: (i) the numerical integration of the system of integro-differential equations given by (22), with the function f satisfying the constraint at the front end and the integral constraint, and η_N computed by iterations; (ii) the solution of Eq. (23) to evaluate the coefficient h_0. Since the function f is monotonic, it results $h_0 > h_f$ with h_0 approaching h_f for large times. The numerical integration of the PDE in Eq. (22) requires an additional condition near the front end, obtained expanding the function $f(\eta)$ to first order in Frobenius series near η_N:

$$f'(\eta_N-\epsilon) = -\frac{\eta_N}{2}, \tag{25}$$

being ϵ a small quantity.

Fig. 5 depicts the prefactor η_N versus β. The improper integral in Eq. (22) was solved numerically approximating the lower limit of integration with a finite quantity l_l. Hence Fig. 5 shows values of η_N for different values of l_l, to check the sensitivity of the solution to this approximation. It is seen that η_N decreases as the cross-section shape becomes flatter, while the influence of the numerical approximation is negligible. The current profile in the moving reference is shown for different values of β in Fig. 6. The profile near the front end of the current is weakly dependent on the cross sectional shape.

Fig. 7 illustrates the extent of the approximation induced by Eq. (15) (hereafter 'approximate model', represented by Eq. (16), against the 'exact model' represented by Eq. (3)) as a function of the similarity variable for a typical set of problem parameters. The numerical integration of the exact model is performed by adopting the technique reported in [29]. In general, the difference between the exact term and its approximate expression is negligible along most of the current profile; near the nose, the approximation introduces an underestimation of the solution for shear thinning fluids, and an overestimation for shear-thickening fluids, whereas the error is null for Newtonian fluids. The error: (i) is larger for small β, corresponding to narrow cross sections; (ii) increases for decreasing bottom inclination θ; (iii) is generally negligible for $\theta > 2°$; (iv) is still limited for $\theta > 0.5°$. The approximated model induces a reduction of the average (negative) shear rate for shear thinning fluids, and an increment of the average shear rate for shear thickening fluids. Since the correction term is significant only in presence of non zero shear rate, we expect that the overall effects of the approximation are limited to the nose of the current and, hence, become progressively less important for long currents, characterised by a uniform thickness for most of their length.

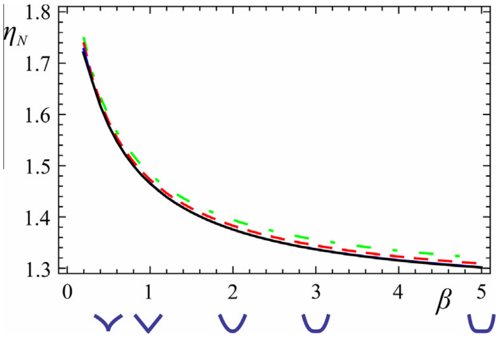

Fig. 5. The prefactor η_N for various shapes of the cross-section computed integrating numerically the system in Eq. (22). The curves refer to different values of the lower limit of integration: −40 (dashdotted), −100 (dashed), −1000 (dotted), −10 000 (continuous).

To appreciate the effect of the approximation on the current profile, the reader is referred to Section 5.2 discussing the experimental results. Fig. 13 therein shows the comparison between the thickness of the current, computed at different times with the approximate and the exact models. It is confirmed that the difference between the results of the two models reduces over time, with the approximate model profiles characterised by a smaller space gradient respect to the exact model. In passing, note that the approximate model performs better than the exact one in comparison with the experiments. This is because in the experiments the vertical velocity of the advancing fluid is not negligible near the source and at early times, and acts in smoothing the space gradient of the current profiles, mimicking the approximate model. See [29] for a discussion on the role and importance of the vertical velocity components in free-surface flows in porous media. It is also noted that at large times (long currents) the front end position is almost unaffected by the approximation, while at smaller times

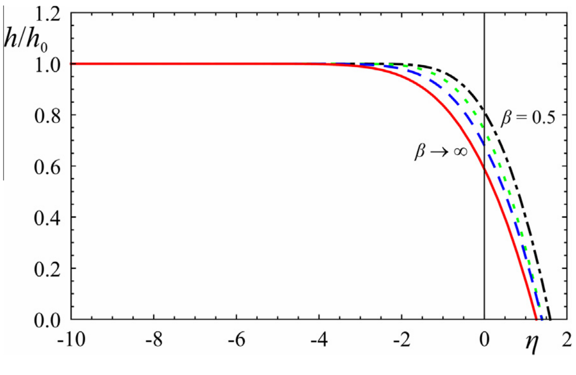

Fig. 6. The dimensionless depth of a constant flux current propagating downslope in a porous channel of power-law cross section described by β. The curves are for $\beta = 0.5$ (dashdotted), $\beta = 1$ (dotted), $\beta = 2$ (dashed), and $\beta \to \infty$ (continuous).

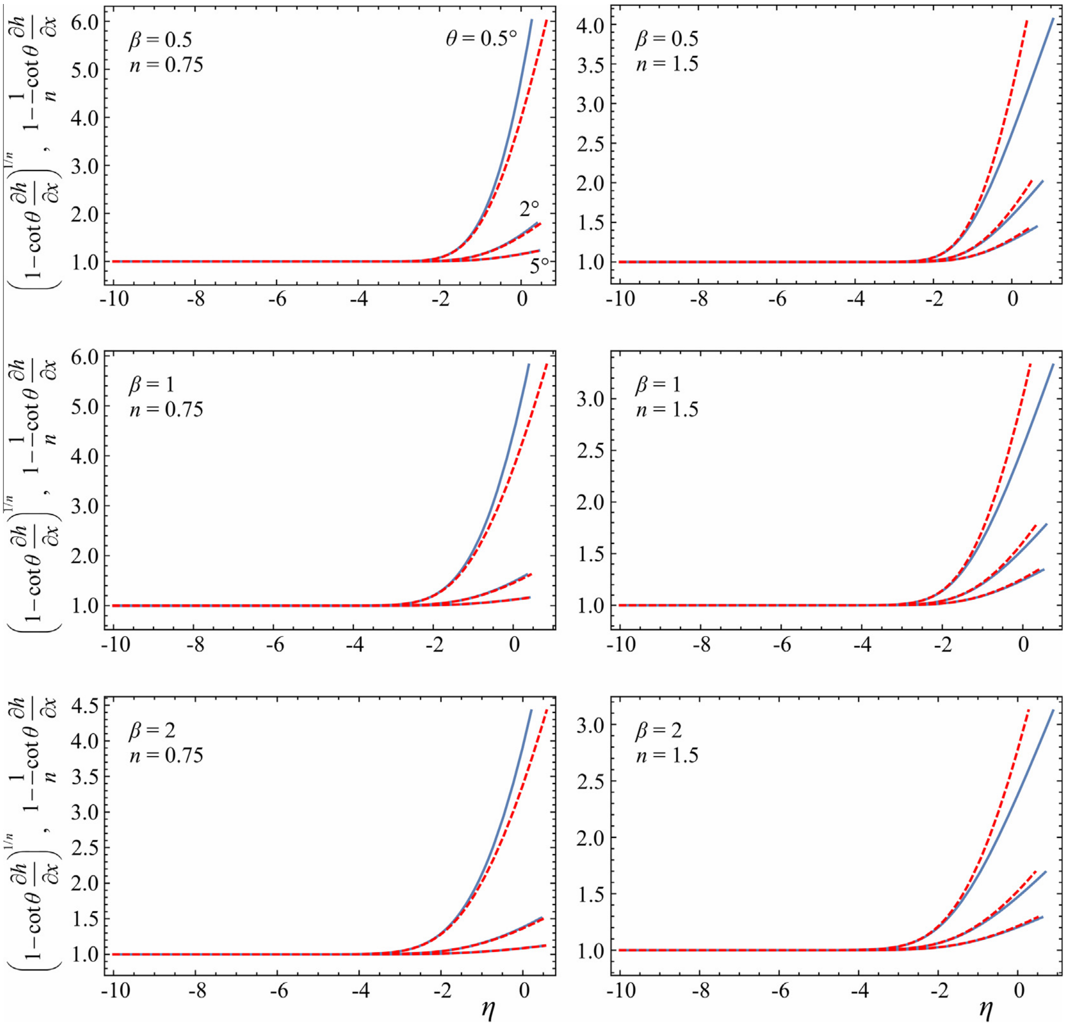

Fig. 7. Comparison between the term $(1 - \cot\theta\partial h/\partial x)^{1/n}$ (continuous curve) and $1 - (1/n)\cot\theta(\partial h/\partial x)$ (dashed curve) for $\beta = 0.5, 1, 2$, $\theta = 0.5°, 2°, 5°$, $n = 0.75, 1.5$.

(short length currents) there are modest differences between the approximate and the exact model. In many aspects, the contribution of the term $\propto \partial h/\partial x$ is similar to that of surface tension effects: it acts in rounding the front of the current which otherwise would be vertical. See Eq. (20) and the corresponding discussion.

5. Experiments

5.1. Experimental setup

A series of laboratory experiments was conducted at the Hydraulics Laboratory of the University of Parma to test the theoretical formulation. The experiments were set up as follows. Two channels made of Polymethyl methacrylate (a transparent thermoplastic), and having a 2000 mm length, were set up between two end plates (Fig. 8). The first channel had a triangular shape with a vertex angle of 45°, while the second had a quarter-circle cross-section with a 95 mm radius. These two cross sections are respectively equivalent to the triangle with a vertex angle of 90° and to a semicircle, due to the symmetry with respect to the median vertical plane and to the negligible influence of the wall boundary layer at said plane. The first channel represents the case $\beta = 1$, while the second approximates the case $\beta = 2$ when the current height is small compared to the channel radius. Both channels lay on four adjustable feet and were levelled to the horizontal or inclined to the desired inclination angle in the longitudinal direction, using an electronic spirit level with an overall accuracy of 0.1°.

The porous medium was created upon gently pouring glass ballotini of uniform diameter in the channel, and letting the medium compact under the action of gravity. Four different diameters of the ballotini ($d = 1, 2, 3, 4$ mm) were employed to reproduce four different media, each with beads of uniform size. The medium porosity was determined performing specific preliminary tests aimed at reproducing how the glass beads used to fill the channel deposit themselves. The porosity values thus determined did not differ significantly between the four media (the differences were within the experimental error), hence an average value $\phi = 0.38$ was assumed, close to that adopted in the experiments by Golding and Huppert [15]. To ensure the porosity value to be spatially uniform and constant for all tests, (i) the protocol adopted to create the porous medium in the preliminary tests was retained across the experiments; (ii) the channels were gently shaken after pouring the beads. The Kozeny–Carman equation, $k = \phi^3 d^2/[180(1-\phi)^2]$, was used to evaluate the medium permeability.

In all experiments, an intruding current of non-Newtonian fluid displaced the air saturating the porous medium. To investigate the impact of the rheology, glycerol, water and Xanthan gum were mixed in various proportions to obtain four different shear-thinning fluids. These had a flow behaviour index, a consistency index and a density in the respective ranges

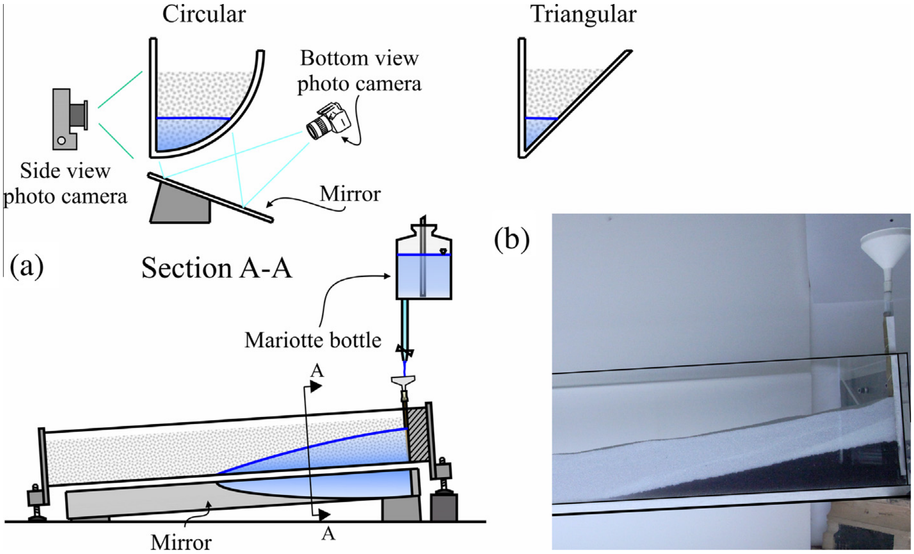

Fig. 8. (a) A schematic of the experimental apparatus. (b) A snapshot of a constant volume flux current propagating in a triangular inclined channel filled with a uniform porous medium. The image refers to Exp. #38.

$n = 0.42 - 0.75, \widetilde{\mu} = 0.015 - 0.67\,\text{Pa}\,\text{s}^n$ and $\rho = 1080 - 1174\,\text{kg}\,\text{m}^{-3}$. In particular, 60% (vol) glycerol, 40% (vol) water, 0.1% (weight) Xanthan gum resulted in the fluid with $n = 0.42$; 50% (vol) glycerol, 50% (vol) water, 0.1% (weight) Xanthan gum resulted in $n = 0.66$; 30% (vol) glycerol, 70% (vol) water, 0.06% (weight) Xanthan gum in $n = 0.70$; 50% (vol) glycerol, 50% (vol) water, 0.01% (weight) Xanthan gum in $n = 0.75$.

The rheology of the fluid was assessed independently with a parallel plate rheometer in the low shear-rate range ($\dot{\gamma} < 5\,\text{s}^{-1}$), with an associated uncertainty equal to $\approx 2.7\%$ and $\approx 3.4\%$ respectively for the fluid behaviour and consistency indexes. The mass density was measured by a pycnometer with an absolute uncertainty of 1 kg m^{-3} and the temperature was controlled with a mercury-in-glass thermometer (0.02 °C resolution).

For both channel shapes, constant volume ($\alpha = 0$) and constant flux ($\alpha = 1$) currents were tested. In both cases, the fluid was injected through an injection zone shaped as a vertical cylinder of diameter 9.5 mm, set at one end of the channel and delimited by a brass net. In the vicinity of the source inlet, the flow-field has a 3-D structure; however this effect rapidly dissipates downstream, considering that the representative width of both channels was of the same order of the length scale of the cylinder. Moreover, 3-D effects are much less relevant for gravity flows in porous media than for gravity currents with a free surface; consequently, the need for a source inlet covering the entire width of the tank (e.g. [30]) is lessened. In particular, the effect of a strongly distorted inflow on gravity-driven flow in porous media was studied by Lyle et al. [9]. The authors concluded that the flow field alterations induced by the position of the inlet are minor, except near the source, and do not modify the subsequent evolution of the current.

For constant volume experiments, a volume of liquid varying from 237 to 916 ml was poured from a beaker into a funnel connected to the injection zone through a short tube; the injected volume was measured by weighing the initial and final volume in the beaker and dividing by the mass density, with an overall uncertainty $\approx 1\%$. The time needed to release the volume was less than 20 s in the most critical conditions (large volume and small glass beads, Exp. #34). This time span is negligible respect to the duration of the experiments (the shorter one, Exp. #13, lasted 710 s) and the current quickly lost memory of the injection details. For

Table 2

Parameter values used for experiments. The symbol 'a' indicates a test of the series reported in Ciriello et al. [28], the symbol * indicates that a video is available as supplementary material. In the second column the symbol 'c' indicates a semicircular cross-section with radius $r = 95$ mm, the symbol 't' indicates a triangular cross-section with vertex angle 45° (i.e. a right triangular section).

Exp.	Shape	θ (deg)	α	d (mm)	q (ml $\text{s}^{-\alpha}$)	n	$\widetilde{\mu}$ (Pa s^n)	ρ (kg m^{-3})
1a	c	0.0	1	2	0.734	0.42	0.36	1160
2a	c	0.0	1	2	1.04	0.42	0.36	1160
3a	c	0.0	1	2	0.68	0.42	0.67	1160
4a	c	0.0	1	3	0.46	0.42	0.67	1160
5a	c	0.0	1	3	0.43	0.66	0.33	1135
6a	c	0.0	1	3	0.275	0.66	0.33	1135
7a	c	0.0	1	4	0.233	0.66	0.33	1135
8a	c	0.0	1	4	0.428	0.66	0.34	1136
9a	c	0.0	1	1	0.43	0.66	0.3	1136
10a	c	0.0	1	1	0.305	0.7	0.067	1080
11a	c	0.0	1	1	0.14	0.75	0.018	1135
12a	c	0.0	1	3	0.583	0.75	0.023	1135
13	c	0.0	0	4	400	0.7	0.067	1080
14	c	0.0	0	2	280	0.7	0.067	1080
15	c	0.0	0	3	500	0.7	0.067	1080
16	c	0.0	0	2	288	0.66	0.34	1136
17	c	0.0	0	4	400	0.66	0.15	1174
18	c	0.0	0	2	237	0.66	0.15	1174
19*	c	0.0	0	3	279	0.66	0.15	1174
20	c	5.2	1	2	1.33	0.75	0.0225	1135
21	c	5.3	1	1	0.55	0.75	0.0225	1135
22	c	5.3	1	3	1.46	0.75	0.0285	1135
23	c	5.2	1	4	2.8	0.75	0.0309	1135
24	c	3.1	1	3	1.05	0.75	0.0309	1135
25	c	3.1	1	1	1.09	0.75	0.0225	1135
26	c	3.1	1	2	0.78	0.75	0.0225	1135
27	c	3.1	1	4	0.67	0.75	0.0309	1135
28	t	0.0	1	2	0.44	0.75	0.015	1135
29*	t	0.0	1	4	0.43	0.66	0.25	1134
30	t	0.0	1	3	0.4	0.66	0.26	1134
31	t	0.0	1	1	0.36	0.66	0.26	1134
32	t	0.0	0	3	372	0.66	0.26	1134
33	t	0.0	0	4	916	0.66	0.26	1134
34	t	0.0	0	2	813	0.66	0.26	1135
35	t	5.4	1	4	1.35	0.75	0.0195	1134
36	t	5.2	1	3	0.86	0.75	0.0215	1134
37	t	3.2	1	2	0.86	0.75	0.0215	1135
38	t	3.2	1	1	0.71	0.75	0.0195	1134

constant volume flux experiments, a flow rate varying from 0.36 to 2.08 ml s^{-1} was supplied by means of a Mariotte bottle equipped with a solenoidal control valve. The injected flow rate was determined before testing, with an overall uncertainty equal to $\approx 2\%$, by weighing the volume of fluid exiting the bottle during a given time interval. The measure was repeated at the beginning and end of each test.

The distance of the current from the injection cross section was recorded at intervals of $10 - 60$ s by means of a high-resolution photo camera. A second photo camera recorded lateral views of the current at its intersection with the vertical plate delimiting the channel along its axis; the resulting images were analysed using a proprietary software to transform the pixel positions into metric coordinates and detect the current profile, with an overall uncertainty of 1.5 mm. The resulting data were space averaged over ten diameters, and adjusted for the effect of the capillary fringe, following the procedure developed by Longo et al. [22].

A total of 38 experiments were performed with the two different cross-sections, horizontal and inclined channels, a constant volume ($\alpha = 0$) and a constant volume flux ($\alpha = 1$). The subset of 12 experiments conducted by our group with $\alpha = 1$ in a horizontal semicircular channel, already discussed in [28], is complemented by 26 additional experiments with both $\alpha = 0$ and $\alpha = 1$. All 38 experiments are listed in Table 2 and discussed in the following.

5.2. Results and discussion

The non dimensional scaled experimental position of the current front x_N is displayed in Fig. 9 against time for horizontal channels of semicircular cross section ($\beta = 2$) for the two cases of constant volume flux ($\alpha = 1$, left panel) and constant volume ($\alpha = 0$, right panel), along with the corresponding theoretical predictions. Similar results are shown in Fig. 10 for horizontal channels of triangular cross-section. While the experimental data

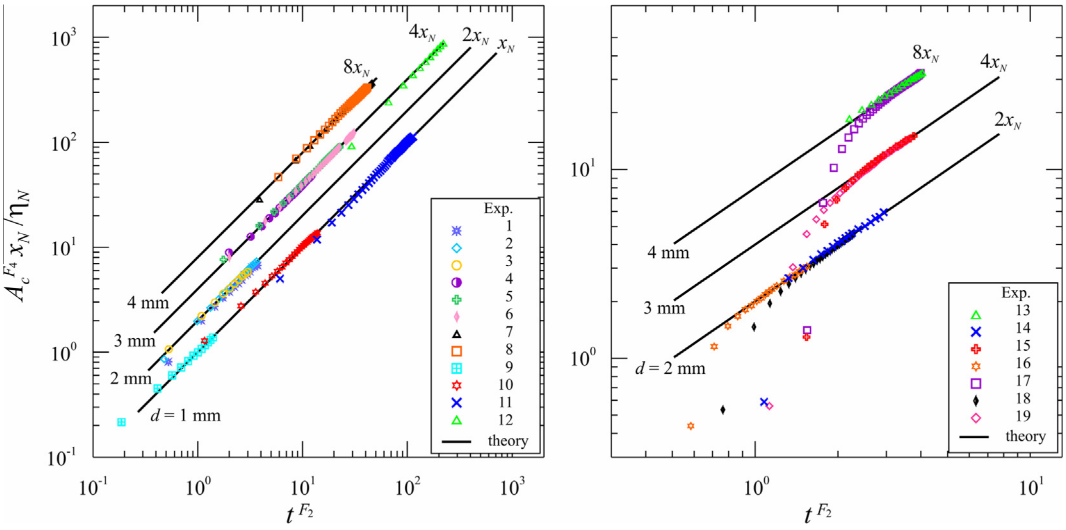

Fig. 9. Experimental (symbols) and theoretical (solid lines) results for the horizontal semicircular channel; scaled non dimensional front position x_N against non dimensional time. Left panel: experiments with constant volume flux ($\alpha = 1$); right panel: experiments with constant volume ($\alpha = 0$). The front end positions (measured and theoretical) have been multiplied by 2 for tests with $d = 2$ mm, by 4 for tests with $d = 3$ mm, and by 8 for tests with $d = 4$ mm, in order to be separated in the diagram. The data in the left panel were already presented in [28] and are shown for comparison.

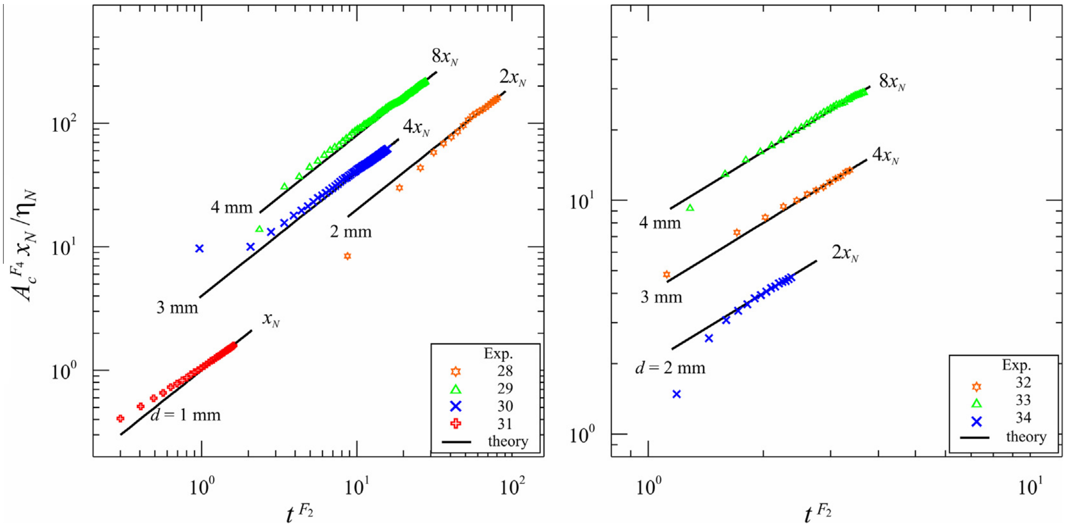

Fig. 10. Same as Fig. 9 but for the horizontal triangular channel. Left panel: experiments with constant volume flux ($\alpha = 1$); right panel: experiments with constant volume ($\alpha = 0$). The front end positions (measured and theoretical) have been multiplied by 2 for tests with $d = 2$ mm, by 4 for tests with $d = 3$ mm, and by 8 for tests with $d = 4$ mm, in order to be separated in the diagram.

differ from the theoretical predictions at early time, the agreement is very good at late time; this holds true for both the time exponent (represented by the inclination of the theoretical curve in log–log scale) and the coefficient. Note that the self-similar solution proves useful in interpreting experimental results even outside asymptotic bounds, as $\alpha_\beta < 1$.

It was observed during the experimentation that the profile of the advancing current was quite smooth, especially for tests with the smaller diameters of the ballotini. In experiments with constant volume release, tests with glass beads of the smallest diameter ($d = 1$ mm) were not performed, as the low permeability of the porous medium entailed a rapid growth of the current thickness at early time, with a consequent violation of most model hypotheses, as discussed in Section 3.2. In general it is expected that for currents of constant volume, part of the fluid is entrapped due to capillarity effects and hence is subtracted from the current volume. The correction operated for the capillary fringe is effective in removing these effects, that are not included in the model. These effects are more relevant when the height of the current reduces over time, as is the case for a constant volume injection, and may have contributed to the deviations from the theory observed at early times for $\alpha = 0$. After correcting for capillary effects, a small initial overprediction of theory to experiments is expected for constant volume tests, due to (moderate) inertial effects. No significant inertial effects are expected for constant volume flux experiments. However, the experimental data indicate a non deterministic over- or under-prediction of the theory. This behaviour can be addressed to the numerous physical limitations in reproducing the inflow conditions and ensuring the homogeneity and isotropy of the porous medium. These limitations include possible local porosity gradients of the medium around the injection zone, and the boundary effect of the walls, which locally increase the porosity and favour the onset of preferential paths. At later stages of propagation, the disturbance induced by the source is lost and the current enters

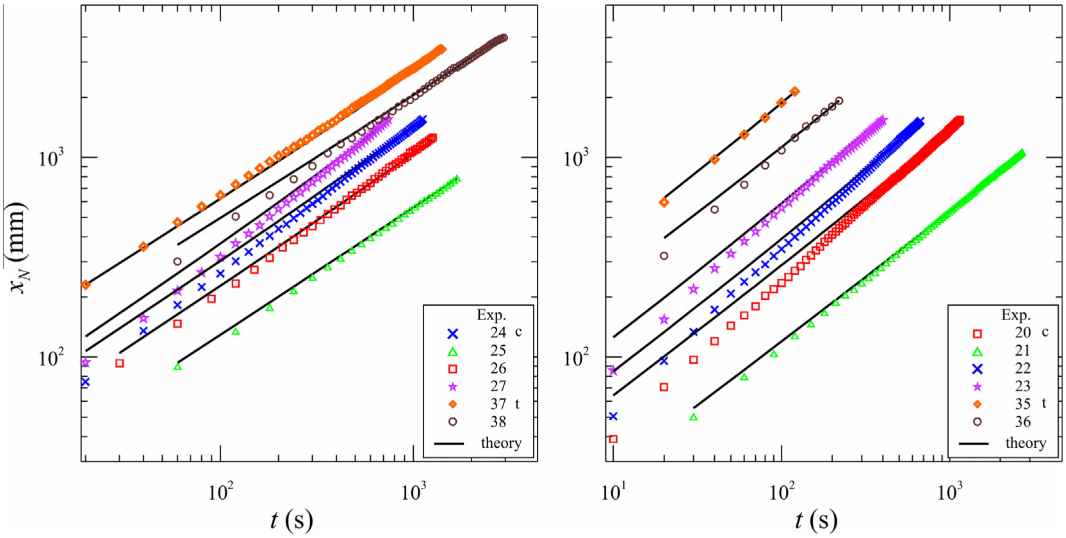

Fig. 11. Experimental (symbols) and theoretical (solid lines) results for inclined semicircular and triangular channels; front position x_N against time for constant volume flux ($\alpha = 1$). Left panel: bottom inclination $\theta = 3.1 - 3.2^\circ$; right panel: $\theta = 5.2 - 5.4^\circ$. The front end positions (measured and theoretical) have been multiplied by 2 for tests with $d = 2$ mm, by 4 for tests with $d = 3$ mm, and by 8 for tests with $d = 4$ mm, in order to be separated in the diagram.

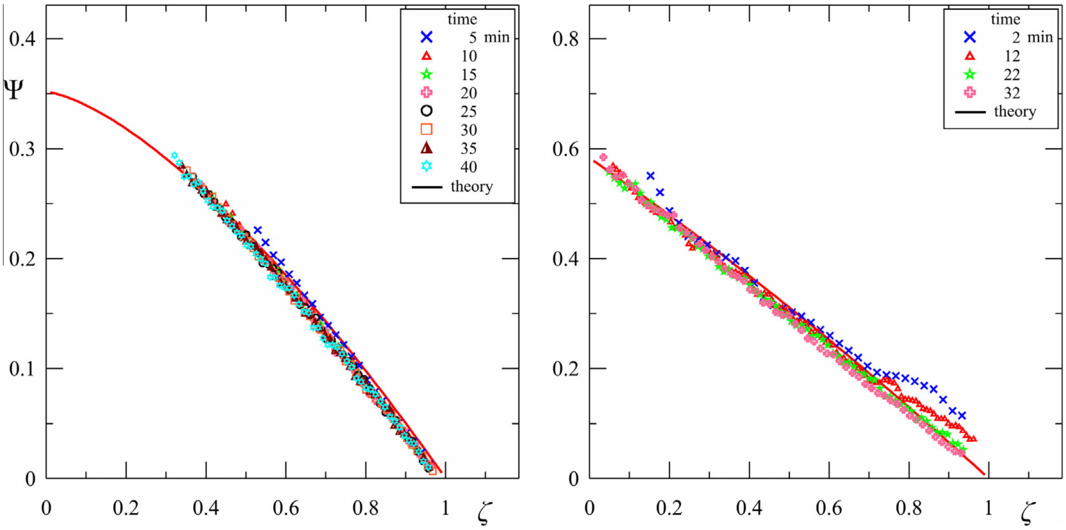

Fig. 12. Experimental (symbols) and theoretical (solid lines) results for horizontal triangular channels; shape function against reduced similarity variable. Left panel: Exp. #34, constant volume ($q = 813$ ml, $d = 4$ mm, $n = 0.66$, $\tilde{\mu} = 0.25$ Pa s^n, $\rho = 1135$ kg m^{-3}). Right panel: Exp. #29, constant volume flux ($q = 0.43$ ml s^{-1}, $d = 2$ mm, $n = 0.66$, $\tilde{\mu} = 0.26$ Pa s^n, $\rho = 1134$ kg m^{-3}). For clarity, only one point of every ten is plotted.

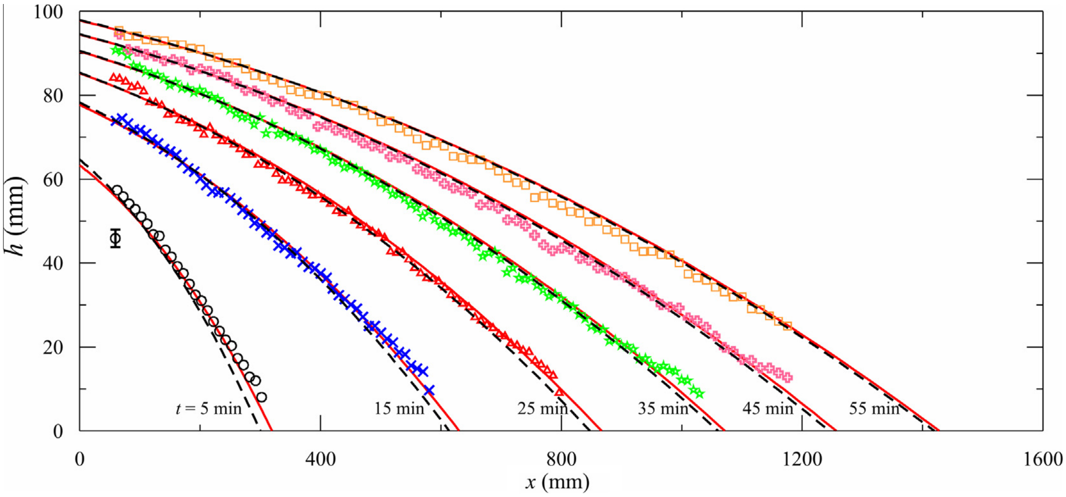

Fig. 13. Experimental (symbols) and theoretical (red solid lines) results for a constant volume flux gravity current in a triangular channel of inclination $\theta = 3.2^\circ$; dimensional current height against down-channel position at six different times. The dashed black lines are the numerical solution of the differential problem without the approximation in Eq. (15). Exp. #38 ($q = 0.71$ ml s^{-1}, $d = 1$ mm, $n = 0.75$, $\tilde{\mu} = 0.0195$ Pa s^n, $\rho = 1135$ kg m^{-3}). For clarity, only one point of every ten is plotted. The error bar refers to ± one standard deviation.

the intermediate asymptotic regime described by the present theoretical model.

The position of the front end x_N of currents of constant volume flux ($\alpha = 1$) is depicted in Fig. 11 against time for inclined channels of semicircular and triangular shape and two different inclinations. Results are represented in dimensional form since no satisfactory dimensionless formulation was found. The theoretical curves, derived via numerical integration of Eqs. (22) and (23), are not rectilinear on a log–log plot, even though they seem to be. Again, the agreement between theory and experiments is good, with an almost perfect overlap at large time.

The current profile was also recorded and compared with the theory for Exps. #34 and #29. Fig. 12 depicts the experimental shape function against the reduced similarity variable for flows of a shear-thinning fluid in a horizontal triangular channel. The left panel shows results for a constant volume current (Exp. #34); early time data are not shown since they represent the current profile during pouring of the fluid, and thus are not representative of model assumptions. At late time, the agreement between experiments and theory is very good. The profile is slightly lower than predicted by the theory near the front. This effect can be addressed to the increased porosity near the corner due to the presence of the wall; this in turn reduces the steepness of the gradient associated to the flux. Results for constant volume flux (Exp. #29), depicted in the right panel, show again, in general, a good agreement between theory and experiments. Early time discrepancies near the origin and the front tend to become negligible at large time. A comparison between the theoretical and experimental height was also performed for inclined triangular channels, as shown in Fig. 13. The theoretical profile is well reproduced by the experiments, except for data near the current front, with experimental results always within the error bars. The physical explanation is that steady state conditions, with a uniform current thickness far from the nose, are not reached due the finite length of the channel, with a consequent limited time of injection. As a result, the profile of the current near the front end differs from the theory.

6. Conclusion

In this study we have analysed theoretically and experimentally the effects of non-Newtonian fluid behaviour on the propagation of currents in a porous medium confined by symmetric rigid boundaries delimiting a channel of assigned shape. Self-similar scalings were derived for the current length and height for propagation in horizontal and inclined channels, with the scaling exponents being a function of model parameters α (rate of increase of current volume with time), n (flow behaviour index), and β (cross-sectional shape). Results obtained exhibit a partial analogy with free-surface flow in open channels without porous media [27], with differences between the two cases deriving from the momentum equation adopted (Darcy or Navier–Stokes).

The speed, height, and aspect ratio of horizontal currents are influenced by all model parameters. This dependence is modulated by two critical values of α, $\alpha_\beta = n/(n+1)$ and $\alpha_n = (2\beta+1)/\beta$. These threshold values govern the decrease/increase with time of the current height and speed/aspect ratio, respectively. For n in the interval 0.5–1.5 (including shear-thinning, Newtonian and shear-thickening fluids), α_β varies between 0.33 and 0.6; for β in the interval 0.25–2 (narrow fractures to semicircular channels), the corresponding range of α_n is 2.5–6. Hence typical values of α_β and α_n are of order 1/2 and 3, respectively, and the former is much more likely to be exceeded than the latter in environmental flows. When the critical values of α are exceeded, the current does not respect asymptotically model assumptions, i.e.: (i) for $\alpha > \alpha_\beta$, the current profile will eventually spread beyond the channel boundaries; (ii) for $\alpha > \alpha_n$, the thin current approximation will be violated. These are asymptotic limitations, and at finite times, the range of the applicability of the solution is wider; this can be checked following Ciriello et al. [12]. Earlier studies on gravity currents in porous media [8,9,15] have shown that self-similar solutions for the spreading of viscous gravity currents are intrinsically robust, and prove useful in interpreting real data, even outside asymptotic bounds. Additional factors supporting this assumption are:

- Overflow scenarios occur only after a considerable time, when the profile increase is slow and/or the channel cross section is elongated in height.
- The invalidity of the Dupuit approximation: (i) is mitigated by the favourable effect of downward vertical velocities, reducing the current thickness and smoothing the spatial pressure gradient; (ii) is a local phenomenon concentrated near the injection zone, with limited effects on the overall current development.

The propagation of currents in inclined channels is affected mainly by their volume (α) and rheological behaviour (n), with a marginal influence of channel shape (β). Constant flux currents

($\alpha = 1$) reach at long times a steady state condition with a uniform thickness profile except near the front end. In variance with Newtonian fluids, it is necessary to approximate the forcing term of the local mass balance equation to derive a self-similar solution for inclined channels. The extent of this approximation depends on the shape of the cross-section and has opposite sign for shear-thinning and shear-thickening fluids. The approximation generally introduces negligible errors for channels with inclination $\theta > 2^\circ$. For a very small channel inclination $\theta < 0.5^\circ$, the self-similar solution should be used with caution and a fully numerical solution to the problem is preferable. For long-length currents, and when the inclination is larger than a limit value (determined on a case by case basis), the effect of the free-surface slope with respect to gravity is entirely negligible (except at the current front); in this case the uniform thickness of constant flux currents depends only on n.

Laboratory experiments conducted with different fluids ($n = 0.42 - 0.75$) in horizontal and inclined channels of different shape (triangular and semicircular) validated the theoretical formulation for constant volume ($\alpha = 0$) and constant volume flux ($\alpha = 1$). A good agreement was observed in both cases with respect to front position and profile, despite the fact that $\alpha > \alpha_\beta$ for horizontal currents with constant volume flux. The major discrepancies between theory and experiments were observed at early times of propagation, when the methodology of injection and the geometry of the inlet are sources of disturbance for the current spreading. However, the effects of these disturbances disappear at a late stage of propagation.

Overall, the proposed model is robust and displays a good agreement with experimental results in the investigated range of parameters. The non-Newtonian rheology significantly affects model results; hence the adoption of the correct constitutive equation is crucial in predicting both the current extension and shape. The sensitivity to the rheological index n is larger for shear-thinning than for shear-thickening fluids. The influence of the channel shape (parameter β) is significant up to $\beta = 3$, less so for larger values.

In this work, the current was considered to be completely confined by the boundaries. Future analysis will tackle more complex scenarios of possible overflowing in the domain close to the injection source, with a mix of axial and channelised flow. Another possible extension of our work is the inclusion of thermal effects, that prove to be particularly relevant in conjunction with non-Newtonian fluid flow in porous media [31].

Acknowledgements

Support from Università di Bologna RFO (Ricerca Fondamentale Orientata) 2012 and 2013 is gratefully acknowledged. We are grateful to the editor and the reviewers for their comments, which improved substantially the quality of the manuscript.

Appendix A. Supplementary data

Supplementary data associated with this article can be found, in the online version, at http://dx.doi.org/10.1016/j.advwatres.2015.02.016.

References

[1] Simpson JE. Gravity currents in the laboratory, atmosphere, and ocean. Ann Rev Fluid Mech 1982;14:213–34. http://dx.doi.org/10.1146/annurev.fl.14.010182.001241.

[2] Ungarish M. An introduction to gravity currents and intrusions. CRC Press; 2009.

[3] Gastone F, Tosco T, Sethi R. Guar gum solutions for improved delivery of iron particles in porous media (part 1): porous medium rheology and guar gum-induced clogging. J Contam Hydrol 2014;166:23–33. http://dx.doi.org/10.1016/j.jconhyd.2014.06.014.

[4] Tosco T, Papini M, Viggi C, Sethi R. Nanoscale zerovalent iron particles for groundwater remediation: a review. J Clean Prod 2014;77:10–21. http://dx.doi.org/10.1016/j.jclepro.2013.12.026.

[5] Dentz M, Tartakovsky D. Abrupt-interface solution for carbon dioxide injection into porous media. Transp Porous Media 2009;79:15–27. http://dx.doi.org/10.1007/s11242-008-9268-y.

[6] Fahs M, Younes A, Mara TA. A new benchmark semi-analytical solution for density-driven flow in porous media. Adv Water Res 2014;70:24–35. http://dx.doi.org/10.1016/j.advwatres.2014.04.013.

[7] Dussan EB, Auzerais FM. Buoyancy-induced flow in porous media generated near a drilled oil well. Part 1. The accumulation of filtrate at a horizontal impermeable boundary. J Fluid Mech 1993;254:283–311. http://dx.doi.org/10.1017/S0022112093002137.

[8] Huppert HE, Woods AW. Gravity-driven flows in porous layers. J Fluid Mech 1995;292:55–69. http://dx.doi.org/10.1017/S0022112095001431.

[9] Lyle S, Huppert H, Hallworth M, Bickle M, Chadwick A. Axisymmetric gravity currents in a porous medium. J Fluid Mech 2005;543:293–302. http://dx.doi.org/10.1017/S0022112005006713.

[10] Vella D, Huppert HE. Gravity currents in a porous medium at an inclined plane. J Fluid Mech 2006;555:353–62. http://dx.doi.org/10.1017/S0022112006009578.

[11] Bickle M, Chadwick R, Huppert H, Hallworth M, Lyle S. Modelling carbon dioxide accumulation at sleipner: implications for underground carbon storage. Earth Planet Sci Lett 2007;255:164–76. http://dx.doi.org/10.1016/j.epsl.2006.12.013.

[12] Ciriello V, Di Federico V, Archetti R, Longo S. Effect of variable permeability on the propagation of thin gravity currents in porous media. Int J Non-Linear Mech 2013;57:168–75. http://dx.doi.org/10.1016/j.ijnonlinmec.2013.07.003.

[13] Zheng Z, Soh B, Huppert HE, Stone HA. Fluid drainage from the edge of a porous reservoir. J Fluid Mech 2013;718:558–68. http://dx.doi.org/10.1017/jfm.2012.630.

[14] Zheng Z, Christov IC, Stone HA. Influence of heterogeneity on second-kind self-similar solutions for viscous gravity currents. J Fluid Mech 2014;747:218–46. http://dx.doi.org/10.1017/jfm.2014.148.

[15] Golding MJ, Huppert HE. The effect of confining impermeable boundaries on gravity currents in a porous medium. J Fluid Mech 2010;649:1–17. http://dx.doi.org/10.1017/S0022112009993223.

[16] Pegler S, Huppert HE, Neufeld JA. Topographic controls on gravity currents in porous media. J Fluid Mech 2013;734:317–37. http://dx.doi.org/10.1017/jfm.2013.466.

[17] Di Federico V, Archetti R, Longo S. Similarity solutions for spreading of a two-dimensional non-Newtonian gravity current. J Non-Newtonian Fluid Mech 2012;177–178:46–53. http://dx.doi.org/10.1016/j.jnnfm.2012.04.003.

[18] Di Federico V, Archetti R, Longo S. Spreading of axisymmetric non-Newtonian power-law gravity currents in porous media. J Non-Newtonian Fluid Mech 2012;189–190:31–9. http://dx.doi.org/10.1016/j.jnnfm.2012.10.002.

[19] Tosco T, Sethi R. Transport of non-Newtonian suspensions of highly concentrated micro-and nanoscale iron particles in porous media: a modeling approach. Environ Sci Technol 2010;44:9062–8. http://dx.doi.org/10.1021/es100868n.

[20] Sochi T. Non-Newtonian flow in porous media. Polymer 2010;51:5007–23. http://dx.doi.org/10.1016/j.polymer.2010.07.047.

[21] Longo S, Di Federico V, Archetti R, Chiapponi L, Ciriello V, Ungarish M. On the axisymmetric spreading of non-Newtonian power-law gravity currents of time-dependent volume: an experimental and theoretical investigation focused on the inference of rheological parameters. J Non-Newtonian Fluid Mech 2013;201:69–79. http://dx.doi.org/10.1016/j.jnnfm.2013.07.008.

[22] Longo S, Di Federico V, Chiapponi L, Archetti R. Experimental verification of power-law non-Newtonian axisymmetric porous gravity currents. J Fluid Mech 2013;731(R2):1–12. http://dx.doi.org/10.1017/jfm.2013.389.

[23] Fadili A, Tardy P, Pearson J. A 3D filtration law for power-law fluids in heterogeneous porous media. J Non-Newtonian Fluid Mech 2002;106:121–46. http://dx.doi.org/10.1016/S0377-0257(02)00085-X.

[24] Di Federico V, Longo S, Chiapponi L, Archetti R, Ciriello V. Radial gravity currents in vertically graded porous media: theory and experiments for Newtonian and power-law fluids. Adv Water Res 2014;70:65–76. http://dx.doi.org/10.1016/j.advwatres.2014.04.015.

[25] Takagi D, Huppert HE. The effect of confining boundaries on viscous gravity currents. J Fluid Mech 2007;577:495–505. http://dx.doi.org/10.1017/S0022112007005174.

[26] Takagi D, Huppert HE. Viscous gravity currents inside confining channels and fractures. Phys Fluids 2008;20:023104. http://dx.doi.org/10.1063/1.2883991.

[27] Longo S, Di Federico V, Chiapponi L. Non-Newtonian power-law gravity currents propagating in confining boundaries. Environ Fluid Mech 2015. http://dx.doi.org/10.1007/s10652-014-9369-9.

[28] Ciriello V, Longo S, Chiapponi L, Di Federico V. Porous gravity currents of non-Newtonian fluids within confining boundaries. Proc Environ Sci, in press.

[29] Longo S, Di Federico V. Axisymmetric gravity currents within porous media: first order solution and experimental validation. J Hydrol 2014;519:238–47. http://dx.doi.org/10.1016/j.jhydrol.2014.07.003.

[30] Chowdhury M, Testik F. Viscous propagation of two-dimensional non-Newtonian gravity currents. Fluid Dyn Res 2012;44:045502. http://dx.doi.org/10.1088/0169-5983/44/4/045502.

[31] Barletta A, de B. Alves L. On Gill's stability problem for non-Newtonian Darcy's flow. Int J Heat Mass Transfer 2014;79:759–68. http://dx.doi.org/10.1016/j.ijheatmasstransfer.2014.08.051.